RESEARCH ARTICLE

PARP Inhibitor Efficacy Depends on CD8+ T-cell Recruitment via Intratumoral STING Pathway Activation in BRCA-Deficient Models of Triple-Negative Breast Cancer

Constantia Pantelidou[1], Olmo Sonzogni[2], Mateus De Oliveria Taveira[2,3], Anita K. Mehta[4], Aditi Kothari[1], Dan Wang[2,5], Tanvi Visal[1], Michelle K. Li[2], Jocelin Pinto[2], Jessica A. Castrillon[4], Emily M. Cheney[4], Peter Bouwman[6], Jos Jonkers[6], Sven Rottenberg[6,7], Jennifer L. Guerriero[4], Gerburg M. Wulf[2], and Geoffrey I. Shapiro[1,8]

ABSTRACT Combinatorial clinical trials of PARP inhibitors with immunotherapies are ongoing, yet the immunomodulatory effects of PARP inhibition have been incompletely studied. Here, we sought to dissect the mechanisms underlying PARP inhibitor–induced changes in the tumor microenvironment of BRCA1-deficient triple-negative breast cancer (TNBC). We demonstrate that the PARP inhibitor olaparib induces CD8+ T-cell infiltration and activation *in vivo*, and that CD8+ T-cell depletion severely compromises antitumor efficacy. Olaparib-induced T-cell recruitment is mediated through activation of the cGAS/STING pathway in tumor cells with paracrine activation of dendritic cells and is more pronounced in HR-deficient compared with HR-proficient TNBC cells and *in vivo* models. CRISPR-mediated knockout of STING in cancer cells prevents proinflammatory signaling and is sufficient to abolish olaparib-induced T-cell infiltration *in vivo*. These findings elucidate an additional mechanism of action of PARP inhibitors and provide a rationale for combining PARP inhibition with immunotherapies for the treatment of TNBC.

SIGNIFICANCE: This work demonstrates cross-talk between PARP inhibition and the tumor microenvironment related to STING/TBK1/IRF3 pathway activation in cancer cells that governs CD8+ T-cell recruitment and antitumor efficacy. The data provide insight into the mechanism of action of PARP inhibitors in *BRCA*-associated breast cancer.

INTRODUCTION

Triple-negative breast cancer (TNBC) is a highly aggressive and heterogeneous disease that constitutes 10% to 20% of breast cancer cases and is associated with poor overall survival and a high probability of distant recurrence and death (1, 2). Conventional chemotherapy has been the standard of care, but initial remissions are often short, and advanced disease remains incurable (2).

A subset of TNBCs are *BRCA*-associated and are deficient in homologous recombination (HR) repair (2). HR deficiency and inhibition of poly(ADP-ribose) polymerase (PARP) have been shown to produce synthetic lethality by a variety of mechanisms related to catalytic inhibition of the PARP enzyme and trapping of PARP–DNA complexes (3). Consequently, among *BRCA*-associated breast cancers, agents such as olaparib and talazoparib have improved the rates of response and progression-free survival compared with standard chemotherapy (4, 5). Despite this promising therapeutic efficacy, treatment with PARP inhibitors has been complicated by both *de novo* and acquired resistance, which has led to the development of combinations with several HR-disrupting strategies in order to sensitize or resensitize cancer cells (3).

There has also been substantial interest in the combination of PARP inhibition with immune-checkpoint blockade, with combinatorial clinical trials ongoing in breast cancer and other cancer types (6). Reports on the interaction of PARP inhibition with the immune microenvironment have shown variable results in preclinical breast cancer models. In the syngeneic model EMT6, PARP inhibition was shown to decrease T-cell infiltration and increase PD-L1 expression via GSK3β inactivation, contributing to immunosuppression that was reversed by the addition of an anti–PD-L1 antibody. Consequently, the combination of PARP inhibitor therapy with anti–PD-L1 blockade led to tumor growth inhibition (7). In contrast, in a BRCA1-deficient TNBC-humanized mouse xenograft model, PARP inhibition was associated with an increased T-cell infiltrate and activated interferon signaling (8). Of note, long-term PARP inhibition in cell line and tumor xenograft models has not been associated with an increase in mutational load, suggesting alternative mechanisms for immuno-modulatory effects (9). To this end, in DNA damage response–deficient TNBC cells, endogenous S-phase damage was shown to activate the cyclic GMP–AMP synthase (cGAS)/stimulator of interferon genes (STING) pathway of cytosolic DNA sensing, leading to proinflammatory cytokine production (10).

We hypothesized that PARP inhibition might activate STING-dependent signaling in *BRCA*-associated TNBC, leading to an antitumor immune response. Here, we show that treatment with the PARP inhibitor olaparib results in the recruitment of

[1]Department of Medical Oncology, Dana-Farber Cancer Institute and Department of Medicine, Harvard Medical School, Boston, Massachusetts. [2]Division of Hematology/Oncology, Department of Medicine, Beth Israel Deaconess Medical Center and Harvard Medical School, Boston, Massachusetts. [3]Department of Imaging, A.C. Camargo Cancer Center, São Paulo, Brazil. [4]Breast Tumor Immunology Laboratory, Susan F. Smith Center for Women's Cancers, Dana-Farber Cancer Institute, Boston, Massachusetts. [5]Otorhinolaryngology Hospital, The First Affiliated Hospital, Sun Yat-sen University, Guangzhou, Guangdong, China. [6]Division of Molecular Pathology, The Netherlands Cancer Institute, Amsterdam, the Netherlands. [7]Institute of Animal Pathology, Vetsuisse Faculty, University of Bern, Switzerland. [8]Department of Medicine, Brigham and Women's Hospital, Boston, Massachusetts.

Note: Supplementary data for this article are available at Cancer Discovery Online (http://cancerdiscovery.aacrjournals.org/).

C. Pantelidou and O. Sonzogni contributed equally to this work.

J.L. Guerriero, G.M. Wulf, and G.I. Shapiro share senior authorship of this article.

Corresponding Author: Geoffrey I. Shapiro, Dana-Farber Cancer Institute, 450 Brookline Avenue, Mayer 446, Boston, MA 02215. Phone: 617-632-4942; Fax: 617-632-1977; E-mail: geoffrey_shapiro@dfci.harvard.edu

Cancer Discov 2019;9:722–37

doi: 10.1158/2159-8290.CD-18-1218

CD8+ T cells in a BRCA1- and p53-deficient genetically engineered mouse model (GEMM) of TNBC, and that CD8+ T-cell depletion diminishes the antitumor efficacy. Olaparib-induced proinflammatory cytokine production and subsequent T-cell infiltration is dependent on cGAS/STING pathway activation exclusively in tumor cells and is more prominent in HR-deficient compared with HR-proficient TNBC cells and *in vivo* models. Our findings uncover a novel mechanism of action of PARP inhibitors and provide an additional mechanistic rationale for combining PARP inhibition with immunotherapies for the treatment of *BRCA*-associated TNBC.

RESULTS

Efficacy of PARP Inhibition Depends on Recruitment of CD8+ T Cells

We evaluated the efficacy of olaparib in tumors derived from the *K14-Cre-Brca1*$^{f/f}$*;Trp53*$^{f/f}$ immunocompetent GEMM of TNBC, where spontaneous mammary carcinomas develop after approximately 7 months (11). Individual tumors from this model were transplanted to immunocompetent FVB/129P2 syngeneic mice or to severe combined immunodeficient (SCID) mice and were treated with vehicle or olaparib. In immunocompetent mice, olaparib-treated tumors rapidly regressed, and in some mice completely cleared. Although resistance to olaparib, evidenced by tumor progression, developed between 100 and 300 days (Supplementary Fig. S1A), olaparib promoted long-term survival, which was increased 16-fold compared with vehicle (Fig. 1A). Notably, the median survival of olaparib-treated SCID mice was significantly lower (103 days) than the median survival of similarly treated immunocompetent mice (241 days; Fig. 1A), suggesting that an intact immune system is required for an optimal response. To confirm the requirement of an immune response for the antitumor efficacy of olaparib, we treated immunocompetent mice with olaparib in the presence of an anti-CD8 antibody. CD8+ T-cell depletion, as verified by flow-cytometric analysis (Supplementary Fig. S1B), markedly accelerated tumor growth (Supplementary Fig. S1A) and significantly reduced the median survival of olaparib-treated mice from 241 to 139 days (Fig. 1A). These findings corroborate that CD8+ T cells contribute to the therapeutic efficacy of PARP inhibition.

We next sought to define the effects of olaparib on the immune microenvironment of TNBC. IHC analysis of tumors from immunocompetent mice showed that olaparib significantly increases CD3+ and CD8+ T cells as early as 3 days after treatment (Supplementary Fig. S1C), as well as at 5 (Fig. 1B and C) and 10 days (Supplementary Fig. S1C). Importantly, CD8+ T-cell recruitment was accompanied by an increase in granzyme B–positive CD8+ cells (Fig. 1B and C), indicative of cytolytic function. Flow-cytometric analysis of immune cell subsets (see Supplementary Fig. S2A and S2B for gating strategy) in tumors treated with olaparib for 5 days showed that PARP inhibition significantly increases total hematopoietic cell and T-cell counts, as measured by CD45 and CD3 staining, respectively (Fig. 1D). Consistent with our IHC analysis, the proportion of CD8+ T cells among CD45+ and total live events, as well as granzyme B expression, was significantly increased in response to olaparib (Fig. 1D). Although olaparib also increased CD4+ T cells, the proportion of T-regulatory FOXP3+CD4+ T cells (Treg) was not significantly affected (Supplementary Fig. S1D), implying that olaparib might be increasing CD4+ T-helper cells, which could further contribute to an effective immune response. T-cell recruitment and activation in response to olaparib was reproduced in two additional independent experiments (Supplementary Fig. S1E). Olaparib augmented granzyme B expression not only in CD8+ T cells but also in natural killer cells (Supplementary Fig. S1E), suggesting activation of both innate and adaptive immune responses. In addition, as the proportion of tumor cells (EPCAM+) decreased in response to PARP inhibition, the microenvironment became populated with T cells (CD3+) and myeloid cells (CD11b+CD11c+; Fig. 1E; Supplementary Fig. S1D). These results demonstrate that PARP inhibition can activate a productive antitumor immune response in BRCA-deficient breast tumors and that recruitment of cytotoxic CD8+ T cells is required for maximal therapeutic response.

To assess whether T-cell infiltration in response to PARP inhibition also occurs in BRCA-proficient TNBC, we established tumors using the KB1P-G3 cell line, derived from our GEMM, and a BRCA-reconstituted isogenic cell line (Fig. 1F; refs. 12, 13). Treatment with olaparib caused accumulation of significantly higher CD3+, CD8+, and granzyme B–positive CD8+ T-cell proportions in BRCA-deficient KB1P-G3 compared with KB1P-G3 + BRCA1 tumors (Fig. 1G). Therefore, PARP inhibition potently induces cytotoxic T-cell recruitment and activation in BRCA-deficient but not BRCA-proficient TNBC models.

Olaparib Activates the STING Pathway in the *K14-Cre-Brca1*$^{f/f}$*Trp53*$^{f/f}$ TNBC GEMM

The cGAS/STING pathway, triggered by cytosolic DNA, has been established as a critical activator of antitumor

Figure 1. Efficacy of PARP inhibition depends on the recruitment of CD8+ T cells. **A,** Tumor chunks from the *BRCA* GEMM were transplanted in syngeneic FVB/129P2 mice (8–10/group), which were treated with vehicle or olaparib along with an isotype (iso) control or an anti-CD8 antibody. Median survivals are shown in parentheses. Tumors were also transplanted in SCID mice (5–6/group) and treated with vehicle or olaparib. Statistical analysis was performed using the log-rank (Mantel–Cox) test. **B** and **C,** Vehicle (VEH)-treated and olaparib (OLA)-treated tumors were harvested 5 days after treatment, fixed, and subjected to IHC analysis for CD3, CD8, and granzyme B expression. Staining was quantified using Aperio algorithms. Error bars, SD. Statistical analyses were performed using unpaired *t* tests or unpaired *t* tests with Welch correction if variances were significantly different. Representative images are shown at 20× magnification. Scale bars, 200 μm. **D** and **E,** Tumors from vehicle- or olaparib-treated mice ($n = 9$) were harvested 5 days after treatment and analyzed by flow cytometry. Scatter plots show significant increases in CD45+, CD3+, CD8+, and granzyme B+ cells in olaparib-treated animals. Pie charts show the proportions of different cell types (as a percentage of total live events) in the tumor microenvironment. Error bars, SD. Statistical analyses were performed using unpaired *t* tests or unpaired *t* tests with Welch correction. **F,** Immunoblotting for BRCA1 expression in KB1P-G3 and KB1P-G3 + BRCA1 cells. **G,** KB1P-G3 and KB1P-G3 + BRCA1 tumors from 5 vehicle- or olaparib-treated mice were harvested 5 days after treatment and analyzed by flow cytometry. Scatter plots show the percentage of CD3+, CD8+, and granzyme B+ cells. Error bars, SD. Statistical analyses were performed using two-way ANOVA with Sidak *post hoc* test.

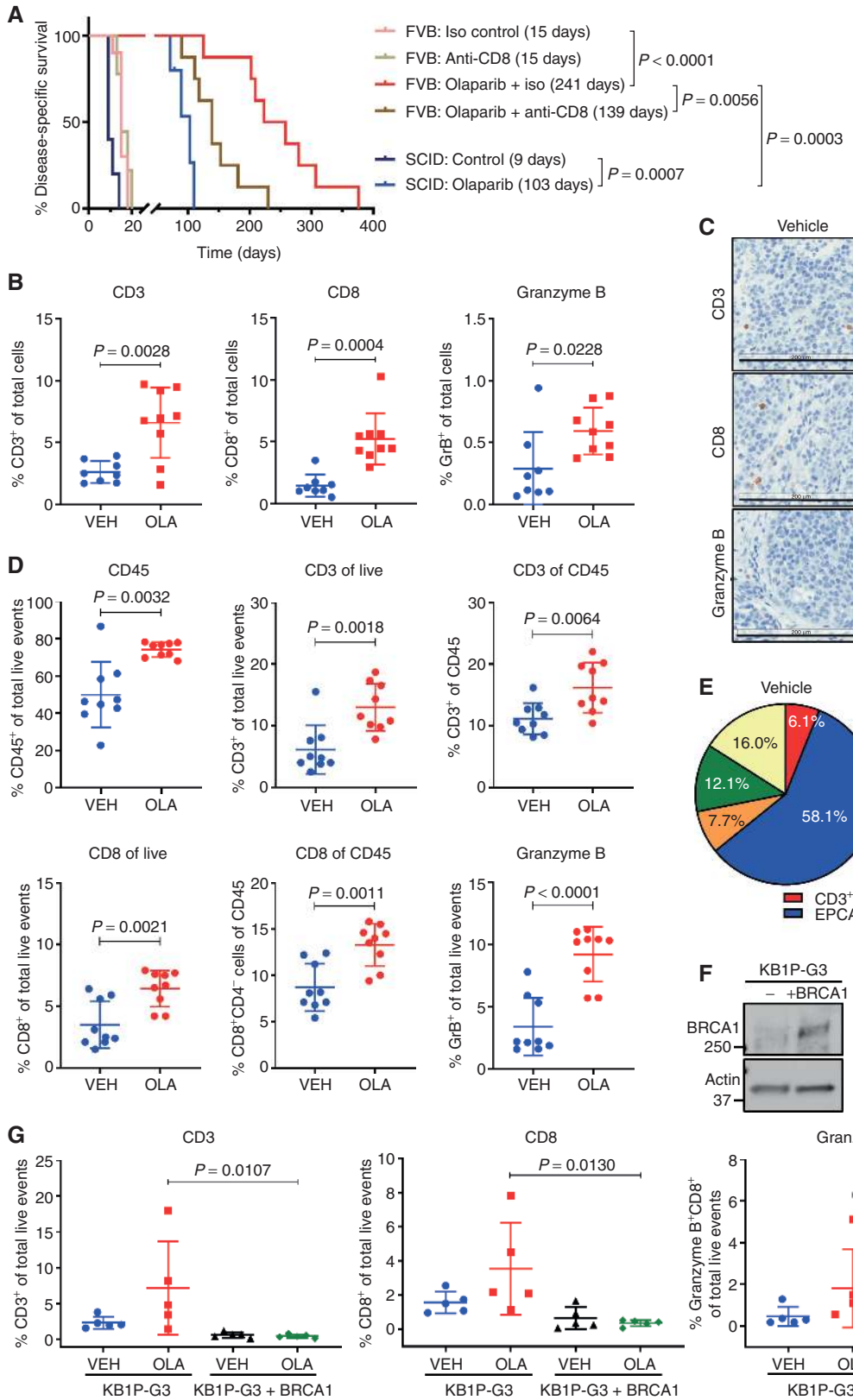

immune responses (14). To determine whether olaparib-induced cytotoxic T-cell recruitment is mediated through cGAS/STING signaling, we examined STING pathway activation in the KB1P-G3 −/+ BRCA1 isogenic paired cell lines. We assessed the presence of cytosolic DNA and observed that the DNA sensor cGAS, which displayed both nuclear and cytoplasmic localization, was found to be associated with cytoplasmic micronuclei (Fig. 2A), previously shown to precede cGAS/STING activation (15). Treatment with olaparib significantly increased formation of cGAS-bound micronuclei in KB1P-G3 but not in KB1P-G3 + BRCA1 cells (Fig. 2A). Next, we assessed the activation of the STING pathway effector TANK-binding kinase 1 (TBK1) by analysis of its activating Ser^{172} phosphorylation (16) and found that olaparib induced TBK1 phosphorylation in KB1P-G3 but not in KB1P-G3 + BRCA1 cells (Fig. 2B). We also measured expression of IFN regulatory factor 3 (IRF3), activated downstream of TBK1 by phosphorylation on Ser^{396} (17). pIRF3 fluorescence intensity was significantly higher in BRCA1-deficient compared with BRCA1-proficient KB1P-G3 cells treated with olaparib (Fig. 2C). We then asked whether TBK1/IRF3 activation correlates with DNA damage accumulation. Formation of γH2AX foci, indicative of DNA strand breaks, was induced in both olaparib-treated KB1P-G3 and KB1P-G3 + BRCA1 cells (Fig. 2C). However, compared with KB1P-G3 + BRCA1, KB1P-G3 cells displayed significantly more γH2AX foci (Fig. 2C). To assess whether olaparib-induced cGAS/STING activation results in proinflammatory cytokine production, we measured expression of IFNβ, known to be primarily induced by STING-dependent signaling (14, 18). Olaparib significantly upregulated the mRNA levels of IFNβ in KB1P-G3 but not in KB1P-G3 + BRCA1 cells (Fig. 2D). We also examined the expression of the proinflammatory chemokines CCL5 and CXCL10, which have been associated with STING/TBK1/IRF3-dependent signaling and T-cell infiltration in TNBC (10, 19–21). Similar to IFNβ, the mRNA levels of CCL5 and CXCL10 were significantly higher in olaparib-treated KB1P-G3 cells compared with their BRCA1-reconstituted pair (Fig. 2D).

We further assessed STING/TBK1/IRF3 pathway activation in K14 cells, another cell line derived from the BRCA1-deficient GEMM (22). We observed a 1,500-fold increase in cGAS-synthesized cGAMP levels following olaparib treatment of K14 cells (Supplementary Fig. S3A). Flow-cytometric analysis of phospho-TBK1^{Ser172}, phospho-IRF3^{Ser396}, and γH2AX (phospho-H2AX^{Ser139}) expression in olaparib-treated K14 cells demonstrated a dose-dependent significant increase, comparable with that of the STING agonist DMXAA (Supplementary Fig. S3B; gating strategy shown in Supplementary Fig. S3C). Increased phosphorylation of IRF3 and H2AX in response to olaparib was confirmed by immunofluorescence microscopy analysis (Supplementary Fig. S3D). Similar to KB1P-G3 cells, olaparib significantly upregulated the mRNA levels of IFNβ, CCL5, and CXCL10 (Supplementary Fig. S3E). Taken together, the data in the KB1P-G3 −/+ BRCA1 and K14 cells indicate that PARP inhibition potently activates the cGAS/STING pathway in BRCA1-deficient but not in BRCA1-proficient murine tumor cells, leading to type I IFN and proinflammatory chemokine production, known to recruit $CD8^+$ T cells (20, 21, 23).

Because the cGAS/STING pathway has previously been shown to be activated in dendritic cells (DC; ref. 14), we assessed whether olaparib activates the pathway in both tumors and DCs *in vivo* by flow-cytometric analysis of harvested tumors treated with vehicle or olaparib (gating strategy shown in Supplementary Fig. S4A and S4B). PARP inhibition significantly increased the proportion of $EPCAM^+pIRF3^+$ cells out of total live events and produced a trend toward increased $EPCAM^+pTBK1^+$ cells, demonstrating activation of STING/TBK1/IRF3 signaling in tumor cells *in vivo* (Fig. 3A). In addition, olaparib significantly increased the proportion of $CD11c^+CD11b^-$ DCs expressing pTBK1 and pIRF3 (Fig. 3B). pTBK1 and pIRF3 levels were also significantly upregulated in DCs expressing major histocompatibility complex class II, indicative of DC maturation and antigen presentation ability (Fig. 3B). The total proportion of mature DCs also increased significantly in response to olaparib (Fig. 3B). Consistent with STING/TBK1/IRF3 pathway activation, mRNA expression analysis of these tumors showed that olaparib increases IFNβ and CCL5 expression (Fig. 3C). Assessment of TBK1/IRF3 signaling in the KB1P-G3 −/+ BRCA1 isogenic tumor model revealed significantly higher proportions of $EPCAM^+pTBK1^+$ and $EPCAM^+pIRF3^+$ tumor cells in olaparib-treated KB1P-G3 tumors compared with KB1P-G3 + BRCA1 (Fig. 3D), consistent with our *in vitro* observations.

To determine whether the observed activation of TBK1/IRF3 signaling in DCs results from a direct effect by PARP inhibitors, we differentiated DCs from bone marrow and cultured them in the presence of olaparib. Although the STING agonist DMXAA potently induced TBK1 phosphorylation in DCs, resulting in their activation ($CD40^+$) and maturation ($MHCII^+$), olaparib did not affect the expression of these markers (Supplementary Fig. S5A and S5B). These findings suggest that PARP inhibition potently activates the cGAS/STING pathway in BRCA1-deficient but not in BRCA1-proficient tumor cells *in vivo*, resulting in subsequent activation of TBK1/IRF3 signaling in DCs that stimulates antigen presentation and consequently $CD8^+$ T-cell infiltration and activation.

Olaparib Activates the STING Pathway More Potently in HR-Deficient Human TNBC Cells Than in HR-Proficient Cells

We next assessed the ability of olaparib to activate the cGAS/STING pathway in human TNBC cells. We utilized the BRCA1-deficient MDA-MB-436 cells and its isogenic BRCA1-reconstituted pair (Supplementary Fig. S6A and S6B), as well as MDA-MB-436 cells with acquired olaparib resistance, generated after prolonged PARP inhibitor exposure (Supplementary Fig. S6B; ref. 24). The mechanism of resistance was shown to be associated with *TP53BP1* mutation, facilitating BRCA1-independent end resection, as well as HSP90-mediated stabilization of the mutant form of BRCA1 capable of interacting with PALB2–BRCA2, facilitating RAD51 loading and subsequently HR repair (24). Olaparib significantly increased the number of cGAS-bound micronuclei in MDA-MB-436 control cells, but not in BRCA1-reconstituted or PARP inhibitor–resistant cells (Fig. 4A). Consistent with cGAS activation, cGAMP synthesis was significantly induced in olaparib-treated MDA-MB-436 control cells but not in

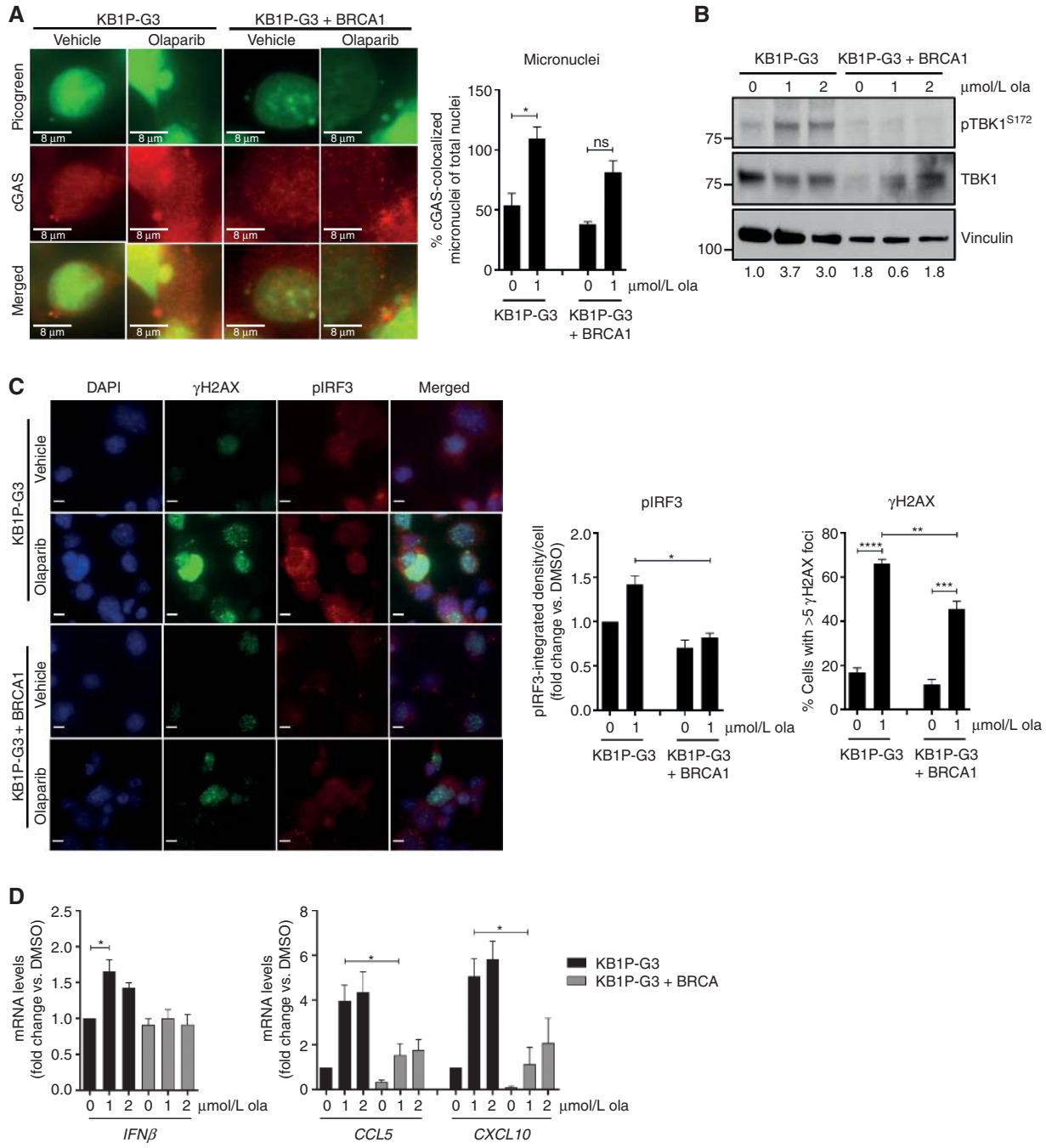

Figure 2. Olaparib activates the cGAS/STING pathway in cells derived from the K14-Cre-*Brca1*$^{f/f}$*Trp53*$^{f/f}$ GEMM. The murine isogenic cell line pair KB1P-G3 −/+ BRCA1 derived from the GEMM was treated with DMSO (0 µmol/L olaparib) or the indicated doses of olaparib (ola). **A,** At 72 hours after treatment, cells were stained with picogreen, fixed, and subjected to immunofluorescence for cGAS. Left, representative images of picogreen (green)- and cGAS (red)-stained micronuclei are shown (60 × magnification). Scale bars, 8 µm. Right, the number of cGAS-colocalized micronuclei was quantified and expressed as a percentage of total nuclei. Error bars, SEM of 2 independent experiments. Statistical analysis was performed using two-way ANOVA with the Tukey *post hoc* test. **B,** At 72 hours after treatment, cells were subjected to immunoblotting for phosphorylated (pTBK1^{Ser172}) and total TBK1 expression with vinculin as a loading control. Markers indicate molecular weight (MW; kDa). Numbers below the blots represent normalized pTBK1 protein levels quantified by densitometric analysis. **C,** At 24 hours after treatment, cells were fixed and subjected to immunofluorescence for γH2AX (pH2AX^{Ser139}) and pIRF3^{Ser396}. Left, representative images of DAPI (blue)-, γH2AX (green)-, and pIRF3 (red)-stained cells are shown (20 × magnification). Scale bars, 8 µm. Right, pIRF3 corrected integrated density/cell was expressed as fold change versus KB1P-G3 DMSO. Statistical analysis was performed using Kruskal–Wallis test with Dunn *post hoc* test. Error bars, SEM of 3 independent experiments. The number of cells displaying >5 γH2AX foci was quantified, and statistical analysis was performed using two-way ANOVA with Tukey *post hoc* test. **D,** At 72 hours after treatment, RNA was extracted and qPCR was performed. *IFNβ*, *CCL5*, and *CXCL10* mRNA levels were normalized to GAPDH internal control. Error bars, SEM of 3–4 independent experiments. Statistical analysis was performed using Kruskal–Wallis test with Dunn *post hoc* test. *, $P < 0.05$; **, $P < 0.01$; ***, $P < 0.001$; ****, $P < 0.0001$.

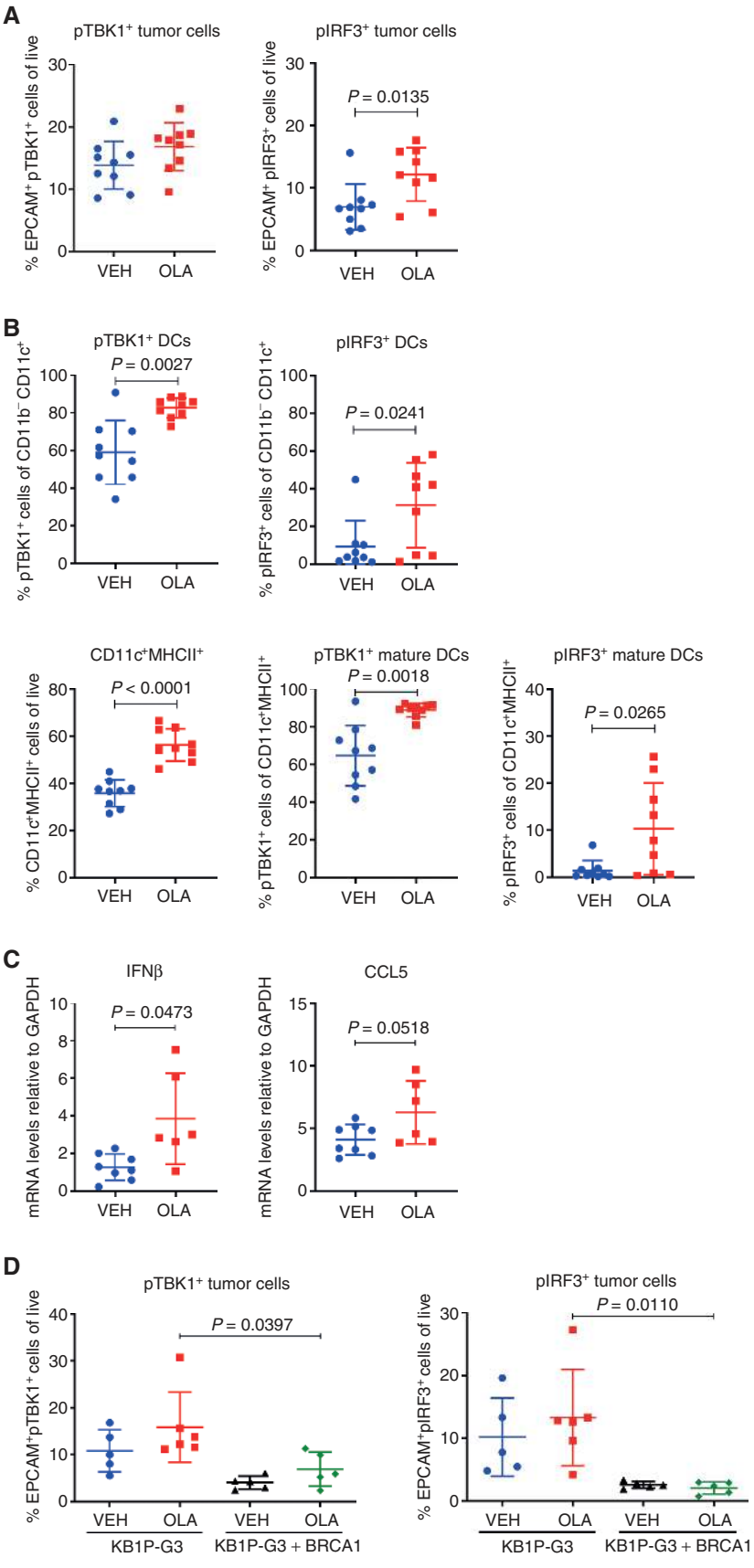

Figure 3. Olaparib induces pTBK1/pIRF3 signaling in tumor and DCs from the K14-Cre-*Brca1*$^{f/f}$*Trp53*$^{f/f}$ GEMM of TNBC. **A** and **B,** Tumors from 9 vehicle- or olaparib-treated mice were harvested 5 days after treatment and subjected to flow cytometry for analysis of pTBK1 and pIRF3 expression. Scatter plots demonstrate increases in (**A**) pTBK1$^+$ and pIRF3$^+$ epithelial (EPCAM$^+$) cells, and (**B**) DCs (CD11b$^-$CD11c$^+$) and mature (CD11c$^+$MHCII$^+$) DCs in olaparib-treated animals. Error bars, SD. Statistical analyses were performed using unpaired *t* tests or unpaired *t* tests with Welch correction. **C,** Tumors from 9 vehicle- or olaparib-treated mice were harvested at 5 days and analyzed for mRNA expression of IFNβ and CCL5 by qPCR. Error bars, SD. Statistical analyses were performed using an unpaired *t* test with Welch correction (left) or an unpaired *t* test (right). **D,** KB1P-G3 and KB1P-G3 + BRCA1 tumors from 5 to 6 vehicle- or olaparib-treated mice were harvested at 5 days after treatment and subjected to flow cytometry. Scatter plots demonstrate the percentage of pTBK1$^+$ and pIRF3$^+$ epithelial (EPCAM$^+$) cells. Error bars, SD. Statistical analyses were performed using two-way ANOVA with Tukey *post hoc* test.

BRCA1-reconstituted or PARP inhibitor–resistant cells (Fig. 4B). Flow-cytometric analysis showed that TBK1 phosphorylation in response to olaparib is impaired in PARP inhibitor–resistant and BRCA1-repleted MDA-MB-436 cells, as compared with parental and control cells (Fig. 4C). The same results were obtained when pTBK1 expression was measured by immunoblotting (Fig. 4D). To confirm these findings, we treated a panel of human TNBC cell lines with olaparib according to their 7-day IC_{50} values (Supplementary Fig. S6B) and assessed pTBK1 expression. In line with our previous observations, olaparib potently induced TBK1 phosphorylation in the HR-deficient MDA-MB-436 cells but not in the *BRCA1* wild-type (WT) HR-proficient MDA-MB-231 cells (Fig. 4E). Less robust TBK1 phosphorylation occurred following olaparib treatment in *BRCA1*-mutant HCC1937 cells, which have previously been shown to retain functional HR proficiency (Fig. 4E; ref. 25). The same pattern of pTBK1 activation was observed when these three cell lines were treated with the same doses of olaparib (Supplementary Fig. S6C). Of note, STING protein levels did not correlate with pTBK1 activation in these cells (Supplementary Fig. S6C). In fact, STING was overexpressed in PARP inhibitor–resistant MDA-MB-436 cells, suggesting that the inability of PARP inhibition to activate TBK1/IRF3 signaling is not a result of reduced STING expression (Supplementary Fig. S6D).

Similar to pTBK1, olaparib significantly increased the proportion of pIRF3-positive MDA-MB-436 parental and control cells, but not of BRCA1-reconstituted or PARP inhibitor–resistant cells (Fig. 4F). Cisplatin, used as a positive control, induced pIRF3 to the same extent as olaparib (Fig. 4F). Additionally, pIRF3 fluorescence intensity as measured by immunofluorescence microscopy was significantly reduced in the presence of BRCA1 expression following treatment with olaparib (Supplementary Fig. S6E). TBK1/IRF3 activation correlated with the induction of DNA damage as measured by flow cytometry (Fig. 4G) and immunofluorescence microscopy (Supplementary Fig. S6E). In agreement with these observations, olaparib significantly stimulated IFNβ production in MDA-MB-436 control cells, but not in BRCA1-reconstituted or PARP inhibitor–resistant cells (Fig. 4H). Although IFNβ expression was exclusively induced in the HR-deficient parental MDA-MB-436 cells, there was a

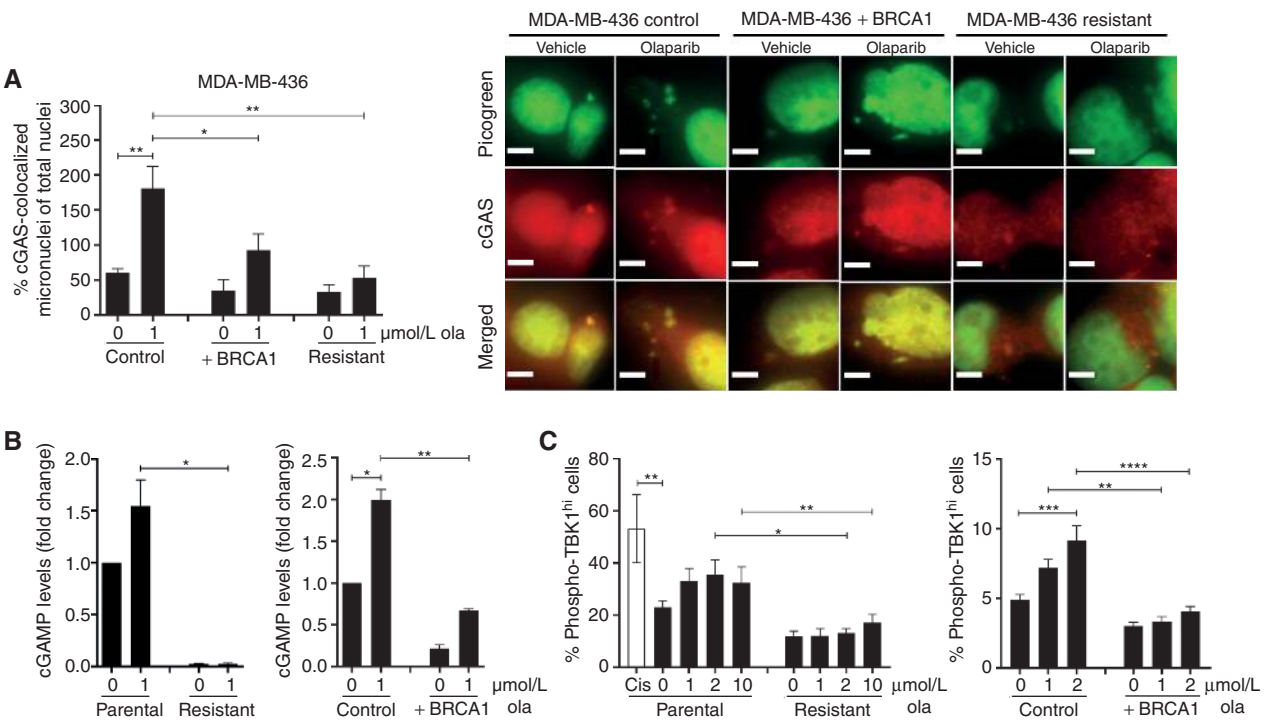

Figure 4. Olaparib activates the STING pathway more potently in HR-deficient TNBC cells compared with HR-proficient cells. **A,** The human TNBC isogenic cell line pair MDA-MB-436 control and BRCA1-reconstituted (+BRCA1) and a PARP inhibitor–resistant MDA-MB-436 clone were treated with DMSO (0 µmol/L olaparib) or the indicated doses of olaparib for 72 hours and subjected to immunofluorescence with picogreen dye and anti-cGAS antibody. Left, quantification of micronuclei. Error bars, SEM of 3 independent experiments. Statistical analysis was performed using one-way ANOVA with Sidak *post hoc* test. Right, representative images of picogreen (green) and cGAS (red) stained micronuclei are shown (60 × magnification). Scale bars, 8 µm. **B,** At 72 hours after treatment with DMSO or olaparib, lysates from parental and PARP inhibitor–resistant MDA-MB-436 cells, as well as MDA-MB-436 control and BRCA1-reconstituted (+BRCA1) cells were subjected to ELISA for cGAMP production. cGAMP levels were expressed as fold change versus DMSO. Error bars, SEM of 2 independent experiments. Statistical analysis was performed using Kruskal–Wallis test with Dunn *post hoc* test. **C**, The same cell lines were treated as in **B** and subjected to flow-cytometric analysis of $pTBK1^{Ser172}$ expression. Cisplatin (cis; 1 µmol/L) was used as positive control. Error bars represent SEM of 2 to 4 independent experiments. Statistical analysis was performed using one-way ANOVA with Sidak *post hoc* test (left) or two-way ANOVA with Tukey *post hoc* test (right). (*continued on next page*)

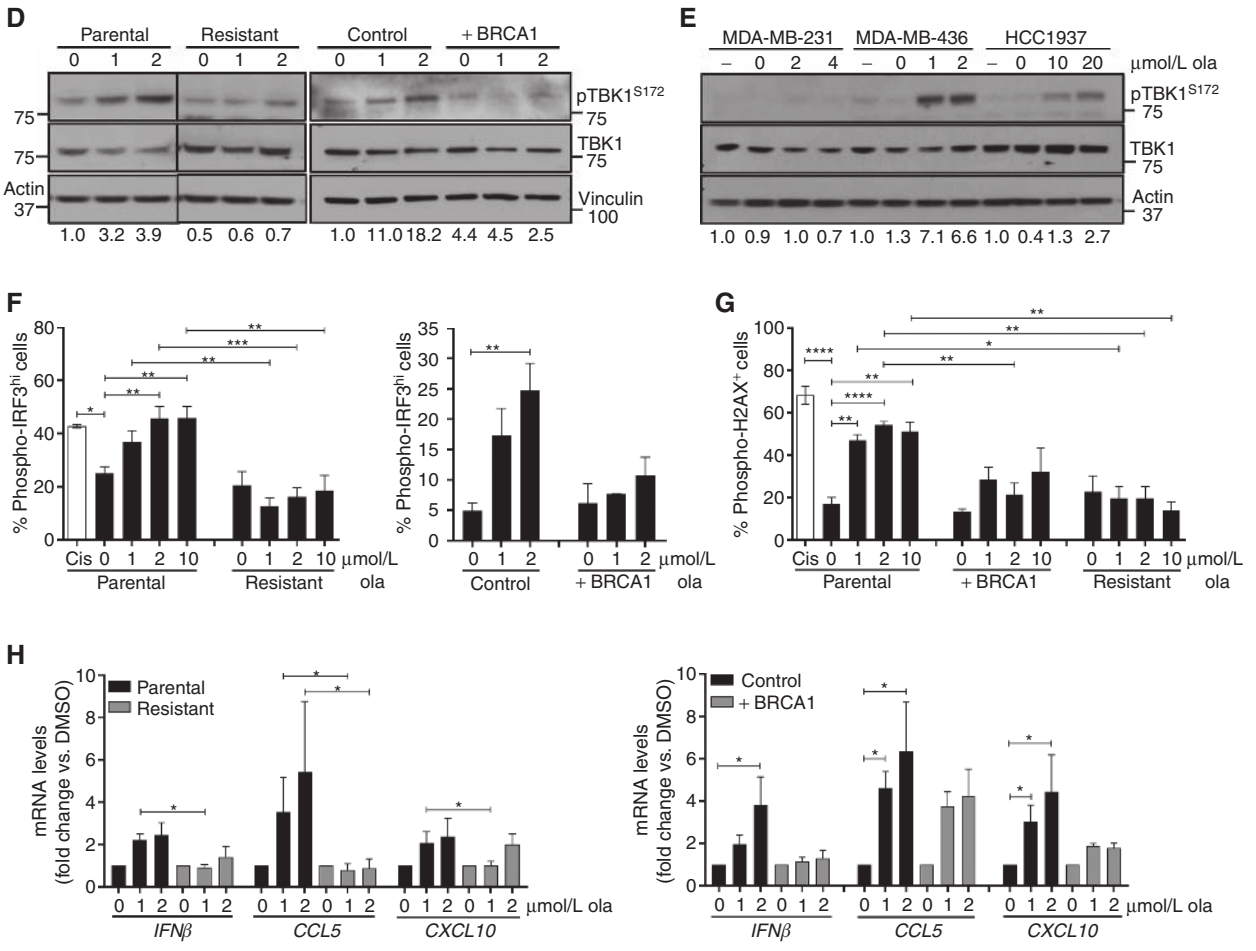

Figure 4. ***(Continued)*** **D,** Cell lines were treated with DMSO or the indicated concentrations of olaparib for 72 hours and lysates were subjected to immunoblotting for pTBK1^{Ser172} and total TBK1 expression. Vertical black lines indicate points of blot cropping. **E,** MDA-MB-436, HCC1937, and MDA-MB-231 human TNBC cell lines were treated with olaparib according to their 7-day IC_{50} values and subjected to immunoblotting for pTBK1^{Ser172} and total TBK1 expression. **F** and **G,** Parental, PARP inhibitor–resistant, control, and BRCA1-reconstituted MDA-MB-436 cells were subjected to flow-cytometric analysis for pIRF3^{Ser396} and pH2AX^{Ser139} expression. Cisplatin (cis; 1 µmol/L) was used as a positive control. Error bars, SEM of 2 to 4 independent experiments. Statistical analysis was performed using one-way ANOVA with Sidak *post hoc* test or two-way ANOVA with Tukey *post hoc* test. **H,** qPCR analysis of *IFNβ*, *CCL5*, and *CXCL10* mRNA levels in parental, PARP inhibitor–resistant, control, and BRCA1-reconstituted MDA-MB-436 cells, normalized to GAPDH internal control. Error bars, SEM of 4 independent experiments. Statistical analyses were performed using Kruskal–Wallis test Dunn *post hoc* test. *, $P < 0.05$; **, $P < 0.01$; ***, $P < 0.001$; ****, $P < 0.0001$.

trend toward increased CCL5 and CXCL10 production in the BRCA1-reconstituted HR-proficient cells (Fig. 4H), suggesting that these chemokines are possibly induced by a STING-independent mechanism. IRF3 activation and proinflammatory cytokine production in response to olaparib was also evident in HCC1937 cells (Supplementary Fig. S6F).

Moreover, we confirmed that cGAS/STING pathway activation is not specific to olaparib and that the PARP inhibitors veliparib and talazoparib also induce cGAMP synthesis, TBK1 phosphorylation, and proinflammatory cytokine production more potently in BRCA-deficient compared with BRCA-proficient cells (Supplementary Fig. S7A–S7D). In summary, these data suggest that PARP inhibitors activate the STING/TBK1/IRF3 pathway and subsequent type I IFN production more potently in HR-deficient compared with HR-proficient human TNBC cells, and this correlates with induction of DNA damage more than with STING protein expression.

Intratumoral STING Pathway Activation Is Required for Olaparib-Induced T-cell Recruitment and Antitumor Efficacy

In order to assess the requirement of STING pathway activation in tumor cells for the production of proinflammatory cytokines in response to PARP inhibition, we used CRISPR/Cas9-mediated knockout (KO) of STING in the K14 cell line derived from the *BRCA* GEMM. CRISPR-mediated KO of STING (STING KO), confirmed by immunoblot analysis (Fig. 5A), did not affect the efficacy of olaparib *in vitro* (Supplementary Fig. S7E). However, olaparib-induced TBK1 phosphorylation was completely abolished in STING-depleted cells compared with the CRISPR/Cas9 control cells (Fig. 5A). The same result was obtained in response to veliparib and talazoparib (Fig. 5A; IC_{50} values are shown in Supplementary Fig. S7E). Consequently, IFNβ, CCL5, and CXCL10 production in

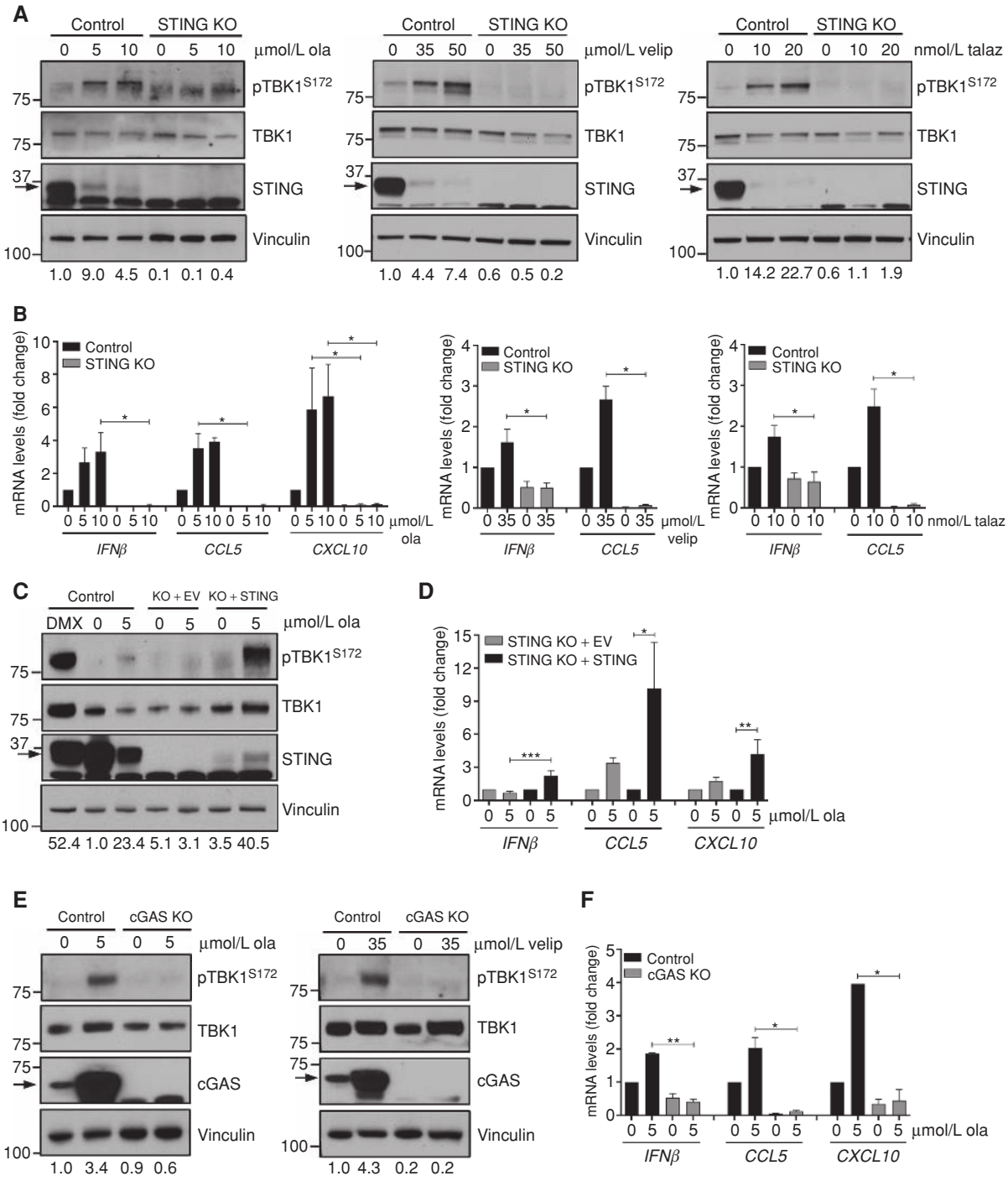

Figure 5. STING or cGAS depletion abolishes olaparib-induced proinflammatory signaling. **A** and **B,** Murine K14 CRISPR/Cas9 control or STING knockout (STING KO) cells were treated with DMSO (0 µmol/L) or the indicated doses of olaparib (ola), veliparib (velip), or talazoparib (talaz) for 72 hours and subjected to immunoblotting or qPCR. STING depletion, as shown by immunoblotting for total STING levels, abolishes PARP inhibitor–induced TBK1 phosphorylation and upregulation of *IFNβ*, *CCL5*, and *CXCL10* mRNA levels, as measured by immunoblotting and qPCR, respectively. Arrows on the blots indicate specific bands and markers indicate MW (kDa). Error bars, SEM of 3 independent experiments. Statistical analyses were performed using Kruskal–Wallis test with Dunn *post hoc* test. **C** and **D,** K14 CRISPR/Cas9 control, STING KO with empty vector (KO + EV) or STING KO with STING-repletion (KO + STING) cells were treated with DMSO or olaparib for 72 hours and subjected to immunoblotting or qPCR. DMXAA (DMX; 10 µmol/L) was used as a positive control. STING repletion in KO cells, as shown by immunoblotting for total STING levels, rescues olaparib-induced TBK1 phosphorylation and induction of *IFNβ*, *CCL5*, and *CXCL10* mRNA expression. Error bars, SEM of 3 independent experiments. Statistical analyses were performed using Kruskal–Wallis test with Dunn *post hoc* test. **E** and **F,** K14 CRISPR/Cas9 control or cGAS KO cells were treated with the indicated doses of olaparib or veliparib for 72 hours and subjected to immunoblotting or qPCR. cGAS depletion, as shown by immunoblotting for cGAS levels, abolishes PARP inhibitor–induced TBK1 phosphorylation and upregulation of *IFNβ*, *CCL5*, and *CXCL10* mRNA levels, as measured by immunoblotting and qPCR, respectively. Error bars, SEM of 3 independent experiments. Statistical analyses were performed using Kruskal–Wallis test with Dunn *post hoc* test. *, $P < 0.05$; **, $P < 0.01$; ***, $P < 0.001$.

response to olaparib, veliparib, and talazoparib (Fig. 5B) was blocked in cells lacking STING, indicating that PARP inhibitor–induced proinflammatory cytokine production is mediated through the STING/TBK1/IRF3 pathway. Of note, total STING protein levels were decreased in response to PARP inhibition, likely due to a negative feedback loop leading to STING degradation, as previously reported (26–28).

STING repletion in the KO cells (KO + STING) rescued olaparib-induced TBK1 phosphorylation as compared with STING KO cells with empty vector (KO + EV; Fig. 5C). pTBK1 induction in olaparib-treated STING-repleted cells resembled pTBK1 levels in DMXAA-treated control cells (Fig. 5C). Reconstitution of STING expression in the KO cells also rescued type I IFN and proinflammatory chemokine production (Fig. 5D). To determine whether the DNA sensor cGAS is necessary for PARP inhibitor–induced TBK1/IRF3 signaling, we depleted cGAS from K14 cells. As seen with STING depletion, cGAS KO completely impaired olaparib- and veliparib-induced TBK1 activation (Fig. 5E) and increase in expression of proinflammatory cytokines (Fig. 5F), confirming that the cGAS/STING pathway is required for PARP inhibitor–induced proinflammatory signaling.

To assess the requirement of STING pathway activation for PARP inhibitor–induced $CD8^+$ T-cell recruitment *in vivo*, we generated tumors from CRISPR/Cas9 control and STING KO cells in syngeneic mice. The tumors maintained depleted levels of STING (Fig. 6A). We next performed flow-cytometric analysis of harvested control and STING KO tumor treated with vehicle or olaparib for 5 days (gating strategies same as in Supplementary Figs. S2 and S4). Consistent with our previous results, olaparib significantly increased the proportion of infiltrating T cells in the CRISPR/Cas9 control tumors with increased $CD8^+$ T cells and granzyme B production (Fig. 6B). In contrast, olaparib-induced $CD8^+$ T-cell recruitment and granzyme B expression was abolished in the STING KO tumors (Fig. 6B). Importantly, olaparib-induced IRF3 activation in both tumors and DCs was also impaired when STING was depleted, supporting the notion of cancer cell–mediated DC activation (Fig. 6C).

To directly examine the requirement of STING in the antitumor efficacy of olaparib, we treated CRISPR/Cas9 control and STING-depleted tumors with olaparib and measured tumor volume. We observed that the growth of STING KO tumors was delayed compared with control tumors, implying that chronic STING pathway activation might have a protumorigenic role as some studies have suggested (29). Nonetheless, tumor burden in response to olaparib was significantly reduced in mice bearing control tumors, but not STING-depleted tumors, suggesting that STING depletion impairs the efficacy of PARP inhibition (Fig. 6D). These findings demonstrate that tumor cell activation of the STING/TBK1/IRF3 pathway and subsequent production of type I IFNs in response to PARP inhibition is necessary for recruitment and activation of cytotoxic $CD8^+$ T cells and consequent antitumor efficacy.

DISCUSSION

In this work, we provide evidence that PARP inhibition triggers an antitumor immune response in a BRCA1- and p53-deficient model of TNBC through activation of the cGAS/STING pathway of cytosolic DNA sensing, and that the antitumor efficacy of PARP inhibitors is critically dependent on the recruitment of granzyme B–positive $CD8^+$ T cells. We demonstrate that the STING/TBK1/IRF3 pathway is activated *in vivo* in BRCA1-deficient but not BRCA1-proficient tumor cells with subsequent paracrine activation in DCs, and that depletion of STING exclusively in tumor cells is sufficient to abolish PARP inhibitor–induced cytotoxic $CD8^+$ T-cell infiltration and antitumor efficacy.

In other model systems, the PARP inhibitor talazoparib has been associated with an increase in Tregs (30). Despite a substantial increase in total $CD4^+$ T cells, we did not observe a significant change in the numbers of immunosuppressive $CD4^+FOXP3^+$ Tregs in response to olaparib in our model. Further studies will be required to determine the precise effects of PARP inhibition on $CD4^+$ T-cell subsets and the role of $CD4^+$ T-cell infiltration in the antitumor efficacy of PARP inhibitors.

In contrast to our findings, it has recently been reported that olaparib decreases cytotoxic $CD8^+$ T-cell fractions, as measured by mass cytometry by time-of-flight (CyTOF), in the EMT6 model of TNBC, and that the addition of an anti–PD-L1 antibody restores $CD8^+$ T-cell numbers (7). The failure of olaparib to recruit T cells in this model might account for the limited antitumor efficacy that was observed and is likely to be attributed to the BRCA proficiency of this model, where STING pathway induction is substantially less robust than in a BRCA-deficient background. The more pronounced STING pathway activation in BRCA1-deficient tumors may explain the naturally higher lymphocyte infiltration of this subset when compared with other types of breast cancer (10).

Although the predominant cell type that produces type I IFNs in the tumor microenvironment is DCs, other cell types, including tumor cells themselves, are emerging as type I IFN producers (14). It has previously been demonstrated that DNA damage response–deficient breast tumor cells that display endogenous S phase–specific DNA damage activate the STING/TBK1/IRF3 pathway, resulting in proinflammatory cytokine production and T-cell recruitment (10). These findings are consistent with our observations that PARP inhibitor–induced DNA damage, which occurs primarily in S phase, correlates with activation of the cGAS/STING pathway and that this response is more pronounced in HR-deficient compared with HR-proficient TNBC models. This translates to more robust T-cell recruitment and activation *in vivo*. Although PARP inhibition activates the STING pathway in both tumors and DCs *in vivo*, we did not find that olaparib directly induces TBK1/IRF3 signaling in bone marrow–isolated DCs *ex vivo*. These results are indicative of tumor cell–mediated paracrine activation of the TBK1/IRF3 pathway in DCs that stimulates antigen presentation and are consistent with recent findings in BRCA-deficient ovarian cancer syngeneic and GEMM models (31). Consequently, we find that STING-mediated signaling exclusively within tumor cells is necessary and sufficient for the cytotoxic $CD8^+$ T-cell infiltration of olaparib-treated tumors and therapeutic efficacy.

Beyond TNBC, the effects of PARP inhibition on the immune microenvironment and cGAS/STING pathway activation have been shown to extend to other tumor types as well. For example, in the BRCA-deficient ovarian cancer model BR5, talazoparib and veliparib have resulted in increased or unchanged $CD8^+$ T-cell infiltration, respectively

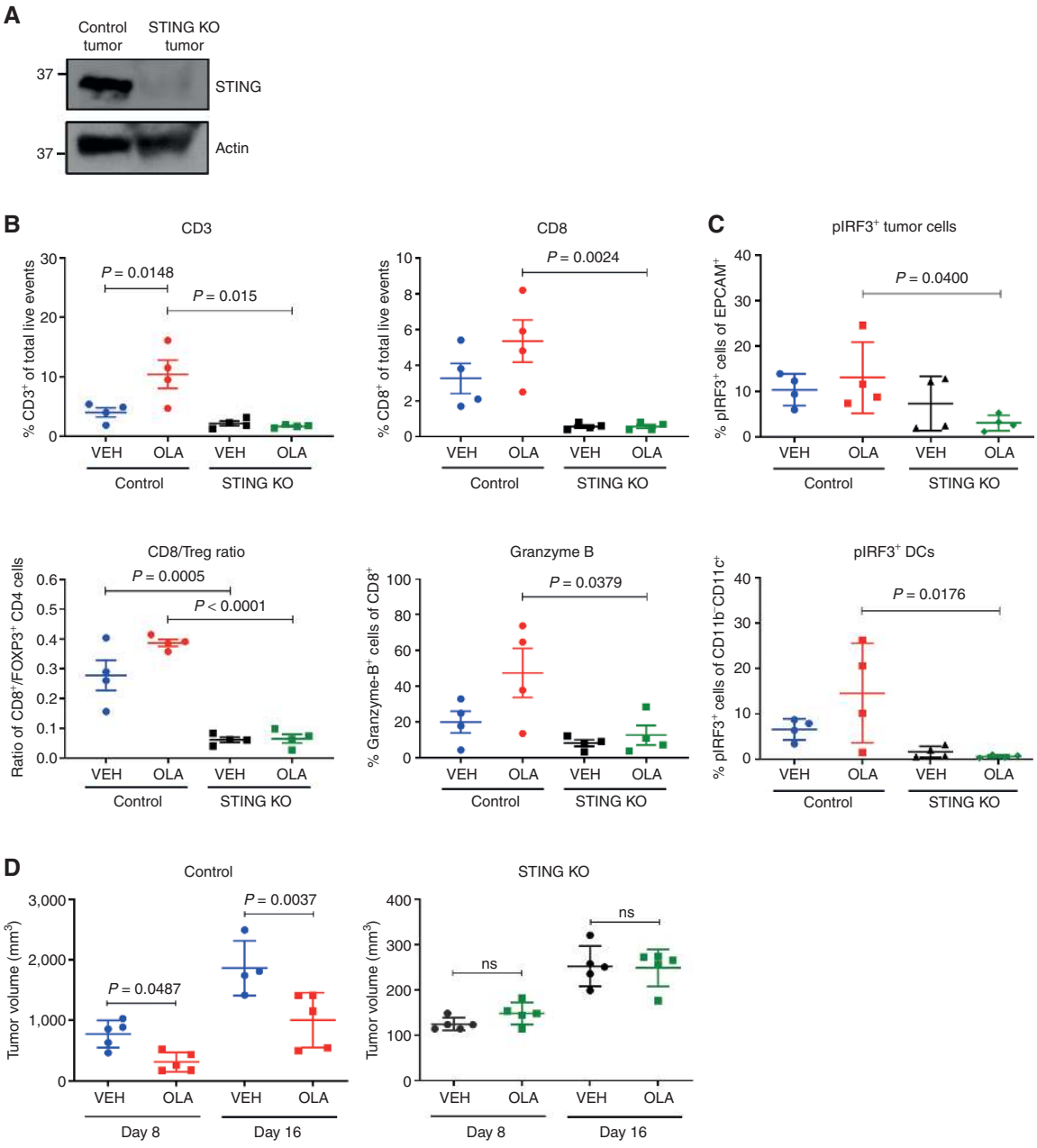

Figure 6. Intratumoral STING depletion abolishes olaparib-induced T-cell recruitment and antitumor efficacy. **A,** Immunoblotting for total STING protein levels in K14 control or STING KO tumors. **B** and **C,** Control and STING KO tumors from 4 mice treated with vehicle (VEH) or olaparib (OLA) for 5 days were subjected to flow cytometry. Scatter plots demonstrate increases in T cells ($CD3^+$, $CD8^+$, and granzyme B^+) and $pIRF3^+$ tumor ($EPCAM^+$) and dendritic ($CD11C^+CD11B^-$) cells in olaparib-treated control but not STING KO tumors. Error bars, SD. Statistical analyses were performed using one-way ANOVA with Sidak *post hoc* test. **D,** K14 CRISPR/Cas9 control or STING KO tumors were transplanted in syngeneic FVB/129P2 mice (5/group), which were treated with vehicle or olaparib. Tumor volumes (mm^3) were measured at days 8 and 16. Error bars, SD. Statistical analysis was performed using one-way ANOVA with Sidak *post hoc* test.

(30, 32), with synergistic immune-mediated tumor clearance afforded by the addition of CTLA4 blockade (32). The survival benefit produced by the CTLA4 combination was T cell–mediated and dependent on increases in IFNγ production (32). Additionally, in the BRCA-proficient ID8 ovarian cancer model, PARP inhibition was shown to activate TBK1/IRF3 proinflammatory signaling with subsequent $CD8^+$ T-cell recruitment. PARP inhibitor efficacy was very modest, although these effects were associated with synergism of PARP inhibition with immune-checkpoint blockade (33). In contrast, although potent STING pathway activation in response to olaparib was observed in DCs derived from ID8/*BRCA1*-null tumors and from a *Trp53*$^{-/-}$, *Brca1*$^{-/-}$, Myc-overexpressing ovarian GEMM, leading to T-cell recruitment, these events did not occur in BRCA-proficient models (31). Taken together, these reports raise the question of the

dependence on BRCA deficiency of PARP inhibitor–mediated immune effects specifically in ovarian cancer. In fact, in the clinical study of combined niraparib and pembrolizumab, responses occurred in patients with ovarian cancer harboring *BRCA* wild-type tumors (34). In the breast cancer models examined here, STING pathway activation and immune responses were clearly more pronounced in the BRCA-deficient setting. Notably, the majority of TNBC clinical responses to niraparib/pembrolizumab occurred among patients harboring *BRCA* mutations (6).

In the ovarian cancer models, the efficacy of olaparib alone or in combination with immune-checkpoint blockade was compromised in STING $^{-/-}$ mice, attributable to a loss of pathway activation in DCs (31, 33). Our results highlight the importance of intratumoral STING in the antitumor effects of olaparib, which stimulates pathway activation in host DCs in a paracrine manner.

Previously, PARP inhibition was shown to be a potential strategy for ERCC1-deficient non–small cell lung cancer (NSCLC; ref. 35). Consistent with the role of the immune system in antitumor activity, PARP inhibition has also been shown to activate a STING-mediated IFN response in ERCC1-deficient NSCLC cells (36). In small cell lung cancer (SCLC) models, olaparib also activates the STING/TBK1/IRF3 pathway. Although olaparib monotherapy did not lead to T-cell recruitment or antitumor efficacy *in vivo*, these effects were reversed by the addition of PD-L1 blockade, and the efficacy of combined olaparib and immune-checkpoint blockade was abolished by STING or cGAS knockdown in tumor cells (37). These results further support the importance of intratumoral STING for the activity of PARP inhibitor–based treatment. Similar findings were observed with the CHK1 inhibitor prexasertib in SCLC models (37), suggesting that STING pathway activation may be a common mechanism among DNA damage–repair inhibitors.

In summary, we have identified CD8$^+$ T-cell recruitment via cancer cell STING pathway activation as a critical determinant of the therapeutic efficacy of PARP inhibition in TNBC. These findings suggest that PARP inhibitors can enhance the antitumor immune response of TNBCs, which has been associated with improved prognosis (38–40). Importantly, these results provide a further mechanistic rationale for combining PARP inhibition with immunotherapy. In a BRCA-deficient background, PARP inhibitor–mediated DNA damage may leverage the STING pathway to convert immunologically cold tumors into hot tumors and sensitize to immune-checkpoint blockade (30, 32). In contrast, in BRCA-proficient tumors, where PARP inhibitor–induced DNA damage and STING-dependent type I IFN responses are limited, a direct STING agonist (41) may be the preferred combinatorial partner with immune-checkpoint blockade.

METHODS

Cell Culture

Human cell lines were purchased from the ATCC between 2015 and 2017, verified with short tandem repeat profiling, maintained in the recommended medium, and passaged up to 15 times. MDA-MB-436 cells with reconstituted BRCA1 expression and with acquired PARP inhibitor resistance have been previously described (24, 42). The K14 cell line was generated by removing breast tumors from *K14-Cre Brca1*$^{f/f}$ *Trp53*$^{f/f}$ females, seeding single-cell suspensions in DMEM (Corning) supplemented with 10% FBS, and passaging until phenotypical and growth rate stability were achieved (22). The murine isogenic cell line pair KB1P-G3 −/+ BRCA1 was generated and maintained as previously described (12, 13). All cell lines were routinely tested for the presence of *Mycoplasma* using the MycoAlert Mycoplasma Detection Kit (Lonza). For flow cytometry, trypsinized cells were incubated in Zombie Aqua Fixable Viability dye (BioLegend) and processed according to the antibody (Supplementary Table S1) manufacturer's protocol ID 407 and 404, for phospho-TBK1 and phospho-IRF3 analysis, respectively.

Viability Assays

Cell viability was assessed by CellTiter-Glo (Promega) according to the manufacturer's guidelines. Viability was normalized to DMSO control and expressed as percentage. Survival curves were generated, and IC_{50} values were derived using nonlinear regression with the equation "[Inhibitor] vs. normalized response − Variable slope" (GraphPad Prism v7).

Compounds

Olaparib (AZD-2281; Selleckchem) and talazoparib (BMN673; Selleckchem) were reconstituted in DMSO (100 mmol/L and 50 mmol/L, respectively). Veliparib (ABT-888; 10 mmol/L) and cisplatin (1 mg/mL) were from Selleckchem and Fresenius Kabi, respectively. DMXAA (S1537; Selleckchem) was reconstituted in DMSO (50 mmol/L).

In Vivo Studies

All animal experiments were conducted in accordance with Institutional Animal Care and Use Committee–approved protocols at Beth Israel Deaconess Medical Center (071-2017) and Dana-Farber Cancer Institute (10-067 and 17-032). Pieces from breast tumors generated in *K14-Cre Brca1*$^{f/f}$*Trp53*$^{f/f}$ female mice were transplanted into the mammary fat pad of FVB/129P2 or SCID/BEIGE (CB17.Cg-*Prkdc*^{scid}*Lyst*$^{bg\text{-}J}$/Crl; Charles River) recipient females that were at least 6 weeks old. FVB/129P2 recipients were generated by breeding FVB females (Jackson Laboratories) and 129P2 males (Envigo) and using the first-generation litters for experimentation. For KB1P-G3 −/+ BRCA1 tumor generation, 5 million cells mixed with Matrigel (Corning) were injected in the mammary fat pad of FVB/129P2 female mice. When tumors reached 15 mm, mice were sacrificed, and tumors were harvested and transplanted into recipient FVB/129P2 females. For efficacy studies, treatments were started once the tumors reached 7 mm in diameter and continued until tumors reached 20 mm in any direction or 1,000 mm^3 in volume, at which point mice were euthanized. For flow cytometry studies, mice bearing tumors of 150 to 300 mm^3 in volume were randomized in treatment groups, so that the average tumor volume in each group was the same. DMSO-reconstituted olaparib was diluted in PBS (Corning) immediately before intraperitoneal injection and administered at 50 mg/kg daily. Anti-CD8 and IgG2b isotype control antibodies (Bio X Cell; #BE0117 and BE0090) were dissolved in PBS (Corning) and administered intraperitoneally at 0.2 mg/dose twice per week. Tumors were measured every 3 to 4 days using electronic calipers, and tumor volumes were calculated by using the ellipsoid formula for volume (L × W × W × pi/6).

IHC

IHC was performed on the Leica Bond automated staining platform. The CD3 antibody (Cell Signaling Technology [CST], #99940 clone D4V8L) and CD8 antibody (CST, #98941 clone D4W2Z) were run at 1:150 and 1:400 dilutions, respectively, using the Leica Biosystems Refine Detection Kit with EDTA antigen retrieval. The

granzyme B antibody (R&D #AF1865 polyclonal) was run at 1:100 dilution using the Leica Biosystems Refine Detection Kit with citrate antigen retrieval. Appropriate control samples were stained using the respective optimized staining protocols, and slides were scanned into the Aperio image analysis platform. Parameters for image analysis macros were developed on the control samples by adapting the membrane v9 or cytoplasmic v2 algorithms as appropriate and used to analyze the CD3, CD8, or granzyme B stains, respectively. IHC analysis of $CD8^+$ cells in Supplementary Fig. S1C was performed by manual counting of $CD8^+$ and total cells in 10 fields/tumor. Images (20× magnification) were acquired using Zeiss Axioimager M1 microscope with Plan-Apochromat 20×/0.8 air.

Tumor Digestion and Flow Cytometry

Mice were sacrificed at the indicated times, and cardiac perfusion was performed. Tumors were extracted, finely minced, blended with the gentleMACS Dissociator (Miltenyi Biotec), and digested with the MACS Miltenyi Tumor Dissociation Kit (Miltenyi Biotec #130-096-730) according to the manufacturer's instructions. Dissociated tumor cells were washed with RPMI-1640 medium and lysed with RBC Lysis Solution (Qiagen). Cells were resuspended in FACS buffer: PBS (Life Technologies) containing 0.5% BSA and 2 mmol/L EDTA (Sigma-Aldrich). The Zombie Aqua Fixable Viability Kit was applied to cells in combination with anti-mouse CD16/CD32 Fcγ receptor II/III blocking antibody (Affymetrix #14-0161-85) for 20 minutes at room temperature, prior to incubation with primary antibodies (Supplementary Table S1) for 1 hour at 4°C. Cells were fixed and permeabilized using the FOXP3/Transcription Factor Staining Buffer Set (Affymetrix #00-5523-00), according to the manufacturer's guidelines, and incubated with antibodies for intracellular antigens overnight at 4°C. The next day, cells were washed, resuspended in PBS, and analyzed using a BD LSRFortessa flow cytometer. Compensation was performed manually on BD FACSDiva using single color and isotype controls, in line with our previous work (43). Signal threshold definition was defined using all-stain, unstained, and isotype controls. Analysis was performed on FlowJo V10. In each experiment, a T-cell panel and a pTBK1-pIRF3 panel were set up; gating strategies for each panel are provided in Supplementary Figs. S2 and S4, respectively.

CRISPR/Cas9-Mediated Knockout, STING Repletion, and Tumor Generation

The guide RNA (gRNA) sequences GTCCAAGTTCGTGCGAGGCTAGG or ATATTCTTGTAGCTCAATCC targeting murine STING or cGAS, respectively, were cloned into the lenti-CRISPR/Cas9v2 vector (Addgene, #52961) according to the Zhang lab protocol (25). The scrambled gRNA sequence CACCGCGTGATGGTCTCGATTGAGT was used as a negative control. Viral infection was performed as described by the RNAi consortium (TRC, Broad Institute) laboratory protocol "Lentivirus production of shRNA or ORF-pLX clones," and single clones were isolated following puromycin selection (2 μg/mL; Sigma-Aldrich #P8833) for 3 weeks. For generation of STING-repleted cells, STING KO cells were transfected with pUNO1-mSTINGwt-HA3x (InvivoGen) or pUNO1 EV using FuGENE 6 transfection reagent (Promega). Plasmid-incorporated cells were enriched by blasticidin selection (30 μg/mL; Life Technologies #A1113903) for 3 weeks, and polyclonal populations were used in experiments. Tumor generation was performed as stated above for the KB1P-G3 model.

Immunofluorescence Microscopy

Cells were seeded on chamber slides (Thermo Scientific Nunc Lab-Tek) and treated as specified. For picogreen-cGAS staining, cells were incubated with pico488 DNA quantification reagent (Lumiprobe Life Science Solutions; 1:500) for 2 hours at 37°C. For all immunofluorescence staining, cells were washed in PBS, fixed in 4% formaldehyde/PBS (10 minutes, room temperature) and permeabilized in 0.25% Triton/PBS (20 minutes, room temperature). Blocking was performed in 5% BSA/0.1% Triton/PBS (30 minutes, room temperature), followed by incubation with primary antibodies (Supplementary Table S1) in blocking buffer (1 hour, 37°C). Cells were washed in PBS and incubated with secondary antibodies (Supplementary Table S1) in blocking buffer (1 hour, room temperature), followed by washing and mounting on coverslips using ProLong Gold antifade reagent with DAPI (#P36935, Life Technologies). Cells were imaged using Nikon widefield confocal microscope at the specified magnification and images were analyzed using ImageJ/Fiji software. For micronuclei and γH2AX foci quantification, at least 50 and 150 nuclei were counted in 5 to 10 fields, respectively. For quantification of fluorescence intensity, the area and integrated density of equally exposed images were measured. Background fluorescence was calculated by measuring the mean gray value from 3 different areas on the image containing no cells. The corrected integrated density was calculated by multiplying the area of the image by the background fluorescence and subtracting the product from the integrated density of the entire image. This was divided by the number of cells in the image to give the corrected integrated density per cell (44).

cGAMP ELISA

cGAMP ELISA (Cayman Chemical) was performed on cell lysates according to the manufacturer's instructions. Briefly, cells were lysed and protein concentration was determined by Bio-Rad protein assay. Titration was performed to determine ideal concentration of protein, which was 25 μg for human and 50 μg for mouse lysates. Two technical replicates were used per biological replicate.

Quantitative PCR

RNA was isolated using the PureLink RNA kit (Invitrogen) and reverse transcribed using the High-Capacity cDNA Reverse Transcription Kit (Applied Biosystems), according to the manufacturer's guidelines. qPCR was performed using Power SYBR Green PCR MasterMix (Applied Biosystems) in a QuantStudio 3 Real-Time PCR System (Applied Biosystems). Primer sequences (5′–3′):

human IFNβ forward AACTTGCTTGGATTCCTACAAAG
and reverse TATTCAAGCCTCCCATTCAATTG,
mouse IFNβ forward CCAGCTCCAAGAAAGGACGA
and reverse CGCCCTGTAGGTGAGGTTGAT,
human CCL5 forward TGCCCACATCAAGGAGTATTT
and reverse CTTTCGGGTGACAAAGACG,
mouse CCL5 forward GCTCCAATCTTGCAGTCGTG
and reverse GCTCCAATCTTGCAGTCGTG,
human CXCL10 forward GGCCATCAAGAATTTACTGAAAGCA
and reverse TCTGTGTGGTCCATCCTTGGAA,
mouse CXCL10 forward CCAAGTGCTGCCGTCATTTT
and reverse CTCAACACGTGGGCAGGATA,
human GAPDH forward GAGTCAACGGATTTGGTCGT
and reverse TTGATTTTGGAGGGATCTCG,
mouse GAPDH forward ACCACAGTCCATGCCATCAC
and reverse TCCACCACCCTGTTGCTGTA.

Bone Marrow–Derived DCs

DCs were derived from FVB/129P2 F1 mice as follows: Using a 25G 5/8″ needled syringe, bone marrow was flushed out of femurs with Hank's Balanced Salt Solution (Gibco) into a 50-mL conical tube. Flushed bone marrow was filtered through a 70-μm cell strainer (Fisherbrand) into another 50-mL tube. Cells were spun down (5 minutes, 1,500 rpm, 4°C), and the pellet was resuspended in ACK buffer (Gibco) to lyse red blood cells. Cells were washed and resuspended

in growing media (RPMI/1% penicillin–streptomycin/0.05 mmol/L 2-mercaptoethanol/10% heat-inactivated FBS; all from Gibco) supplemented with 200 ng/mL FLT3l (PeproTech) for 7 days. At day 7, cells were collected, counted, and seeded in the presence of DMSO, DMXAA (5 μg/mL), or olaparib (5 μmol/L). After 20 hours, cells were collected, resuspended in FACS buffer, and stained for flow cytometry as detailed above ("Tumor digestion and flow cytometry" section).

Immunoblotting

Cells were lysed in RIPA buffer (Boston BioProducts) supplemented with protease and phosphatase inhibitors (Calbiochem), quantitated for protein using the BCA Protein Assay Kit (Pierce), and equal amounts of protein were resolved by SDS-PAGE. Membranes were blocked in 5% milk/TBS-T (Boston BioProducts) and incubated with antibodies (Supplementary Table S1). Immunodetection was performed using SuperSignal West Pico and Femto Chemiluminescent Substrate (Thermo Fisher Scientific). Blot stripping was performed using Restore PLUS Western Blot Stripping Buffer (Life Technologies) according to the manufacturer's guidelines. Protein levels were quantified by densitometric analysis using ImageJ/Fiji. Phosphorylated protein levels were normalized to total protein band, then to loading control, and expressed as fold change versus control DMSO. Immunoblots shown are representative of three independent experiments.

Statistical Analyses

Statistical analyses were performed using GraphPad Prism v7 and v8. For comparison of two sets of measurements, an unpaired *t* test was performed. An unpaired *t* test with Welch correction was used when sample variances were not equal, as defined by the Brown–Forsythe test. For two sets of fold-change measurements, a one-sample *t* test was used (measurements were compared with the value of 1). For comparison of three or more sets of unpaired measurements, one-way ANOVA was performed with Tukey *post hoc* test if all sets were analyzed, or Sidak *post hoc* test if selected relevant pairs were analyzed (as recommended by GraphPad Prism). When the Brown–Forsythe test indicated that sample variances were not equal, the Brown–Forsythe ANOVA test was performed with Games–Howell *post hoc* test. When two variables were present, two-way ANOVA with Tukey *post hoc* test was performed. For comparison of three or more sets of measurements that did not follow a normal distribution, e.g., fold-change measurements, the Kruskal–Wallis test with Dunn *post hoc* test was performed. Normality was examined using the Kolmogorov–Smirnov test. *, $P < 0.05$; **, $P < 0.01$; ***, $P < 0.001$; ****, $P < 0.0001$.

Disclosure of Potential Conflicts of Interest

J.L. Guerriero reports receiving commercial research grants from GlaxoSmithKline and Eli Lilly and has received other remuneration from GlaxoSmithKline. G.M. Wulf reports receiving a commercial research grant from Merck & Co. and has ownership interest in US 20090258352 A1 Pin1 as a marker for abnormal cell growth licensed to Cell Signaling, R&D Systems; Application 14/348810 Compositions and Methods for the Treatment of proliferative diseases is pending. G.I. Shapiro reports receiving commercial research grants from Eli Lilly, Merck EMD-Serono, Merck & Co., and Sierra Oncology and is a consultant/advisory board member for Pfizer, Lilly, Almac, Ipsen, Bayer, Angiex, Daiichi Sankyo, G1 Therapeutics, Roche, Merck EMD-Serono, Sierra Oncology, Bicycle Therapeutics, Fusion Pharmaceuticals, Cybrexa Therapeutics, and Astex. No potential conflicts of interest were disclosed by the other authors.

Authors' Contributions

Conception and design: C. Pantelidou, O. Sonzogni, M. De Oliveria Taveira, J.L. Guerriero, G.M. Wulf, G.I. Shapiro

Development of methodology: C. Pantelidou, O. Sonzogni, A.K. Mehta, D. Wang, S. Rottenberg, J.L. Guerriero, G.I. Shapiro

Acquisition of data (provided animals, acquired and managed patients, provided facilities, etc.): C. Pantelidou, O. Sonzogni, M. De Oliveria Taveira, A.K. Mehta, D. Wang, T. Visal, M.K. Li, J. Pinto, J.A. Castrillon, P. Bouwman, J. Jonkers, J.L. Guerriero, G.M. Wulf, G.I. Shapiro

Analysis and interpretation of data (e.g., statistical analysis, biostatistics, computational analysis): C. Pantelidou, O. Sonzogni, M. De Oliveria Taveira, A.K. Mehta, A. Kothari, D. Wang, T. Visal, M.K. Li, J. Pinto, J.A. Castrillon, J.L. Guerriero, G.M. Wulf, G.I. Shapiro

Writing, review, and/or revision of the manuscript: C. Pantelidou, O. Sonzogni, M. De Oliveria Taveira, A. Kothari, M.K. Li, S. Rottenberg, J.L. Guerriero, G.M. Wulf, G.I. Shapiro

Administrative, technical, or material support (i.e., reporting or organizing data, constructing databases): C. Pantelidou, O. Sonzogni, A. Kothari, T. Visal, M.K. Li, J.A. Castrillon, E.M. Cheney, S. Rottenberg, J.L. Guerriero, G.I. Shapiro

Study supervision: C. Pantelidou, G.M. Wulf, G.I. Shapiro

Acknowledgments

This work was supported by the Dana-Farber/Harvard Cancer Center Specialized Program of Research Excellence (SPORE) in Breast Cancer, P50 CA168504 (G.I. Shapiro and G.M. Wulf); a P50 CA168504 Career Enhancement Award (J.L. Guerriero); NIHR01 CA090687 (G.I. Shapiro); Susan Komen Career Catalyst Award CCR18547597 (J.L. Guerriero); and Merck Investigator Studies Program (MISP) Grant LKR163726 (G.I. Shapiro, G.M. Wulf), as well as the Breast Cancer Research Foundation (G.M. Wulf), the Ludwig Center at Harvard (G.M. Wulf), NIHR01 CA226776 (G.M. Wulf), and ERC CoG-681572 (S. Rottenberg). We thank Shawn Johnson for support with preliminary experiments, Brett Gross for technical help, Liam Cornell for help with CRISPR technology, and Bose Kochupurakkal for assistance with IHC analyses. We thank Dana-Farber/Harvard Cancer Center in Boston, MA, for the use of the Specialized Histopathology Core, which provided histology and immunohistochemistry services. Dana-Farber/Harvard Cancer Center is supported in part by an NCI Cancer Center Support Grant NIH5 P30 CA06516.

Received October 15, 2018; revised April 12, 2019; accepted April 18, 2019; published first April 23, 2019.

REFERENCES

1. Carey L, Winer E, Viale G, Cameron D, Gianni L. Triple-negative breast cancer: disease entity or title of convenience? Nat Rev Clin Oncol 2010;7:683–92.
2. Bianchini G, Balko JM, Mayer IA, Sanders ME, Gianni L. Triple-negative breast cancer: challenges and opportunities of a heterogeneous disease. Nat Rev Clin Oncol 2016;13:674–90.
3. Lord CJ, Ashworth A. PARP inhibitors: synthetic lethality in the clinic. Science 2017;355:1152–8.
4. Robson M, Im S-A, Senkus E, Xu B, mchek S, Masuda N, et al. Olaparib for metastatic breast cancer in patients with a germline BRCA mutation. N Engl J Med 2017;377:523–33.
5. Litton JK, Rugo HS, Ettl J, Hurvitz SA, Gonçalves A, Lee K-HH, et al. Talazoparib in patients with advanced breast cancer and a germline BRCA mutation. N Engl J Med 2018;379:753–63.
6. Vinayak S, Tolaney SM, Schwartzberg L, Mita MM, McCann G, Tan AR, et al. TOPACIO/Keynote-162: Niraparib + pembrolizumab in patients (pts) with metastatic triple-negative breast cancer (TNBC), a phase 2 trial. J Clin Oncol 2018;36:1011[abstract].
7. Jiao S, Xia W, Yamaguchi H, Wei Y, Chen M-K, Hsu J-M, et al. PARP inhibitor upregulates PD-L1 expression and enhances cancer-associated immunosuppression. Clin Cancer Res 2017;23:3711–20.

8. Wang Z, Sun K, Xiao Y, Feng B, Mikule K, Ma X, et al. Niraparib activates interferon signaling and potentiates anti-PD-1 antibody efficacy in tumor models. Sci Rep 2019;9:1853.
9. Póti Á, Berta K, Xiao Y, Pipek O, Klus GT, Ried T, et al. Long-term treatment with the PARP inhibitor niraparib does not increase the mutation load in cell line models and tumour xenografts. Brit J Cancer 2018;119:1392–400.
10. Parkes EE, Walker SM, Taggart LE, McCabe N, Knight LA, Wilkinson R, et al. Activation of STING-dependent innate immune signaling by S-phase-specific DNA damage in breast cancer. J Natl Cancer Inst 2017;109:1–10.
11. Liu X, Holstege H, van der Gulden H, Treur-Mulder M, Zevenhoven J, Velds A, et al. Somatic loss of BRCA1 and p53 in mice induces mammary tumors with features of human BRCA1-mutated basal-like breast cancer. Proc Natl Acad Sci U S A 2007;104:12111–6.
12. Jaspers JE, Kersbergen A, Boon U, Sol W, van Deemter L, Zander SA, et al. Loss of 53BP1 causes PARP inhibitor resistance in Brca1-mutated mouse mammary tumors. Cancer Discov 2013;3:68–81.
13. Barazas M, Gasparini A, Huang Y, Küçükosmanoğlu A, Annunziato S, Bouwman P, et al. Radiosensitivity is an acquired vulnerability of PARPi-resistant BRCA1-deficient tumors. Cancer Res 2018;79:452–60.
14. Corrales L, McWhirter SM, Dubensky TW, Gajewski TF. The host STING pathway at the interface of cancer and immunity. J Clin Invest 2016;126:2404–11.
15. Harding SM, Benci JL, Irianto J, Discher DE, Minn AJ, Greenberg RA. Mitotic progression following DNA damage enables pattern recognition within micronuclei. Nature 2017;548:466–70.
16. Ma X, Helgason E, Phung QT, Quan CL, Iyer RS, Lee MW, et al. Molecular basis of Tank-binding kinase 1 activation by transautophosphorylation. Proc Natl Acad Sci U S A 2012;109:9378–83.
17. Servant MJ, Grandvaux N, tenOever BR, Duguay D, Lin R, Hiscott J. Identification of the minimal phosphoacceptor site required for in vivo activation of interferon regulatory factor 3 in response to virus and double-stranded RNA. J Biol Chem 2003;278:9441–7.
18. Bose D. cGAS/STING pathway in cancer: Jekyll and Hyde story of cancer immune response. Int J Mol Sci 2017;18:2456.
19. Lee H, Lee J-J, Song I, Park I, Kang J, Yu J, et al. Prognostic and predictive value of NanoString-based immune-related gene signatures in a neoadjuvant setting of triple-negative breast cancer: relationship to tumor-infiltrating lymphocytes. Breast Cancer Res Treat 2015;151:619–27.
20. Araujo JM, Gomez AC, Aguilar A, Salgado R, Balko JM, Bravo L, et al. Effect of CCL5 expression in the recruitment of immune cells in triple negative breast cancer. Sci Rep 2018;8:4899.
21. Mulligan A, Raitman I, Feeley L, Pinnaduwage D, Nguyen LT, O'Malley FP, et al. Tumoral lymphocytic infiltration and expression of the chemokine CXCL10 in breast cancers from the Ontario Familial Breast Cancer Registry. Clin Cancer Res 2013;19:336–46.
22. Juvekar A, Hu H, Yadegarynia S, Lyssiotis CA, Ullas S, Lien EC, et al. Phosphoinositide 3-kinase inhibitors induce DNA damage through nucleoside depletion. Proc Natl Acad Sci U S A 2016;113:E4338–47.
23. Hervas-Stubbs S, Perez-Gracia J, Rouzaut A, Sanmamed MF, Bon A, Melero I. Direct effects of type I interferons on cells of the immune system. Clin Cancer Res 2011;17:2619–27.
24. Johnson N, Johnson SF, Yao W, Li Y-C, Choi Y-E, Bernhardy AJ, et al. Stabilization of mutant BRCA1 protein confers PARP inhibitor and platinum resistance. Proc Natl Acad Sci U S A 2013;110:17041–6.
25. Johnson SF, Cruz C, Greifenberg A, Dust S, Stover DG, Chi D, et al. CDK12 inhibition reverses de novo and acquired PARP inhibitor resistance in BRCA wild-type and mutated models of triple-negative breast cancer. Cell Rep 2016;17:2367–81.
26. Prabakaran T, Bodda C, Krapp C, Zhang B, Christensen MH, Sun C, et al. Attenuation of cGAS-STING signaling is mediated by a p62/SQSTM1-dependent autophagy pathway activated by TBK1. EMBO J 2018;37:e97858.
27. Konno H, Konno K, Barber GN. Cyclic dinucleotides trigger ULK1 (ATG1) phosphorylation of STING to prevent sustained innate immune signaling. Cell 2013;155:688–98.
28. Dobbs N, Burnaevskiy N, Chen D, Gonugunta VK, Alto NM, Yan N. STING activation by translocation from the ER is associated with infection and autoinflammatory disease. Cell Host Microbe 2015;18:157–68.
29. Khoo L, Chen L. Role of the cGAS–STING pathway in cancer development and oncotherapeutic approaches. EMBO Rep 2018;19:e46935.
30. Huang J, Wang L, Cong Z, Amoozgar Z, Kiner E, Xing D, et al. The PARP1 inhibitor BMN 673 exhibits immunoregulatory effects in a Brca1$^{-/-}$ murine model of ovarian cancer. Biochem Biophys Res Commun 2015;463:551–6.
31. Ding L, Kim H-J, Wang Q, Kearns M, Jiang T, Ohlson CE, et al. PARP inhibition elicits STING-dependent antitumor immunity in Brca1-deficient ovarian cancer. Cell Rep 2018;25:2972–80.e5.
32. Higuchi T, Flies DB, Marjon NA, Mantia-Smaldone G, Ronner L, Gimotty PA, et al. CTLA-4 blockade synergizes therapeutically with PARP inhibition in BRCA1-deficient ovarian cancer. Cancer Immunol Res 2015;3:1257–68.
33. Shen J, Zhao W, Ju Z, Wang L, Peng Y, Labrie M, et al. PARPi triggers the STING-dependent immune response and enhances the therapeutic efficacy of immune checkpoint blockade independent of BRCAness. Cancer Res 2019;79:311–9.
34. Konstantinopoulos PA, Waggoner SE, Vidal GA, Mita MM, Fleming GF, Holloway RW, et al. TOPACIO/Keynote-162 (NCT02657889): a phase 1/2 study of niraparib + pembrolizumab in patients (pts) with advanced triple-negative breast cancer or recurrent ovarian cancer (ROC)—Results from ROC cohort. J Clin Oncol 2018;36:suppl, A106 [abstract].
35. Postel-Vinay S, Bajrami I, Friboulet L, Elliott R, Fontebasso Y, Dorvault N, et al. A high-throughput screen identifies PARP1/2 inhibitors as a potential therapy for ERCC1-deficient non-small cell lung cancer. Oncogene 2013;32:5377–87.
36. Chabanon RM, Muirhead G, Krastev DB, Adam J, Morel D, Garrido M, et al. PARP inhibition enhances tumor cell-intrinsic immunity in ERCC1-deficient non-small cell lung cancer. J Clin Invest 2019;129:1211–28.
37. Sen T, Rodriguez BL, Chen L, Della Corte CM, Morikawa N, Fujimoto J, et al. Targeting DNA damage response promotes antitumor immunity through STING-mediated T-cell activation in small cell lung cancer. Cancer Discov 2019 ;9:646–61.
38. Loi S, Sirtaine N, Piette F, Salgado R, Viale G, Eenoo F, et al. Prognostic and predictive value of tumor-infiltrating lymphocytes in a phase III randomized adjuvant breast cancer trial in node-positive breast cancer comparing the addition of docetaxel to doxorubicin with doxorubicin-based chemotherapy: BIG 02-98. J Clin Oncol 2013;31:860–7.
39. Ono M, Tsuda H, Shimizu C, Yamamoto S, Shibata T, Yamamoto H, et al. Tumor-infiltrating lymphocytes are correlated with response to neoadjuvant chemotherapy in triple-negative breast cancer. Breast Cancer Res Treat 2012;132:793–805.
40. Kwa M, Adams S. Prognostic and predictive value of tumor-infiltrating lymphocytes in breast cancer. Curr Breast Cancer Rep 2016;8:1–13.
41. Iurescia S, Fioretti D, Rinaldi M. Targeting cytosolic nucleic acid-sensing pathways for cancer immunotherapies. Front Immunol 2018;9:711.
42. Wang Y, Krais JJ, Bernhardy AJ, Nicolas E, Cai KQ, Harrell MI, et al. RING domain–deficient BRCA1 promotes PARP inhibitor and platinum resistance. J Clin Invest 2016;126:3145–57.
43. Guerriero JL, Sotayo A, Ponichtera HE, Castrillon JA, Pourzia AL, Schad S, et al. Class IIa HDAC inhibition reduces breast tumours and metastases through anti-tumour macrophages. Nature 2017;543:428.
44. Ferreira T, Rasband WS. ImageJ user guide-IJ 1.46. Bethesda, MD: NIH; 2010.